Ionospheric plasma fluctuations induced by the NWC very low frequency signal transmitter

Magnus Fagernes Ivarsen[1], Park Jaeheung[2], Yaqi Jin[1], and Lasse Boy Novock Clausen[1]

[1]University of Oslo
[2]Korea Astronomy and Space Science Institute

November 23, 2022

Abstract

The Australian NWC (North West Cape) signal transmitter is known to strongly interfere with the topside ionosphere. We analyze 456 conjunctions between Swarm A, B and NWC, in addition to 58 conjunctions between NorSat-1 and NWC. The in-situ measurements provided by these satellites include the 16 Hz Swarm Advanced Plasma density dataset, and the novel 1000 Hz plasma density measurements from the m-NLP system aboard NorSat-1. We subject the data to a detailed PSD analysis and subsequent superposed epoch analysis. This allows us to present comprehensive statistics of the NWC-induced plasma fluctuations, both their scale-dependency, and their climatology. The result should be seen in the context of VLF signal transmitter-induced plasma density fluctuations, where we find counter-evidence for the existence of turbulent structuring induced by the NWC transmitter.

Ionospheric plasma fluctuations induced by the NWC very low frequency signal transmitter

Magnus F Ivarsen[1], Jaeheung Park[2,3], Yaqi Jin[1], Lasse B N Clausen[1]

[1]Department of Physics, University of Oslo, Oslo, Norway
[2]Korea Astronomy and Space Science Institute, Daejeon, South Korea
[3]Department of Astronomy and Space Science, Korea University of Science and Technology, Daejeon, South Korea

Key Points:

- The NWC transmitter produces clearly observable plasma density fluctuations in the topside F-region ionosphere
- The scale sizes associated with these plasma fluctuations are strongest between 1 km - 10 km
- The NWC-induced plasma fluctuations are most visible during a tenuous ionosphere, and during magnetic midnight

Corresponding author: Magnus F Ivarsen, `m.f.ivarsen@fys.uio.no`

Abstract

The Australian NWC (North West Cape) signal transmitter is known to strongly interfere with the topside ionosphere. We analyze 456 conjunctions between Swarm A, B and NWC, in addition to 58 conjunctions between NorSat-1 and NWC. The in-situ measurements provided by these satellites include the 16 Hz Swarm Advanced Plasma density dataset, and the novel 1000 Hz plasma density measurements from the m-NLP system aboard NorSat-1. We subject the data to a detailed PSD analysis and subsequent superposed epoch analysis. This allows us to present comprehensive statistics of the NWC-induced plasma fluctuations, both their scale-dependency, and their climatology. The result should be seen in the context of VLF signal transmitter-induced plasma density fluctuations, where we find counter-evidence for the existence of turbulent structuring induced by the NWC transmitter.

1 Introduction

Since the late 1800s, radio communication antennae utilize the partial reflection of radio signals off the bottom-side of the ionosphere, enabling long-range communication. However, part of the signal is absorbed by the ionosphere. The electromagnetic waves associated with the radio antennae accelerate and heat plasma, a fact that has been exploited for scientific enquiry numerous times (T. B. Leyser & Wong, 2009; Streltsov et al., 2018, e.g.,).

The effects of radio transmitter signals on the ionosphere by production of a scattered and reflected signal are detected using ground-based instruments. Here, very high frequency or ultra high frequency radar transmitters are frequently used as incoherent scatter radars (Folkestad et al., 1983; Stubbe & HagforS, 1997). Conversely, radar receivers can record the effect of pre-existing structuring of ionospheric plasma on radio signals, by examining the rapid scintillations in radio signal phase and amplitude caused by changes in local plasma refractive index (Yeh & Liu, 1982; Kintner P. M. et al., 2007; Jin et al., 2017). Lastly, the effects by radio signal transmission of heating or accelerating plasma can readily be scrutinized in-situ, using sounding rockets or satellites (T. Leyser, 2001; Chernyshov et al., 2016; Streltsov et al., 2018).

In the latter category, very low frequency (VLF) radio signal transmitters are primarily used for long-range naval communication. While the study of VLF signals originating in space are vital to understanding radiation belt dynamics (Graf et al., 2013), terrestrial VLF transmitters induce observable changes in radiation belt precipitation (Inan et al., 1984; Cohen & Inan, 2012).

Recently, several studies have investigated the impact on the ionosphere by the Australian NWC (North West Cape) VLF radio transmitter complex. NWC operates at a frequency of 19.8 kHz, and, like other VLF communication transmitters, operate at a particularly high power, exceeding 1 MW. As such, and since it is continuously operating, it has a clearly observable effect on the overhead ionosphere, as illustrated in Fig. 1, showing in-situ plasma observations that will be defined in the Methodology section.

Zhao et al. (2019) studied VLF signals from several ground-based stations, including NWC, using data from the Chinese ZH-1 satellite. The authors found evidence of ionospheric heating, both magnetic and electric field perturbations, and precipitation caused by NWC at an altitude of 507 km. Mishin et al. (2010) and Xia et al. (2020) studied spectral broadening in the NWC signal at an altitude of 600 km, using data from the DEMETER satellite. Mishin et al. (2010) concluded that interactions between the NWC signal and ionospheric plasma resulted in non-linear plasma instabilities, giving rise to turbulence, and ultimately causing a loss of VLF signal. Xia et al. (2020) found that these effects are strongest on the nightside and during times with a low ambient electron density. Němec et al. (2020) likewise used data from the DEMETER satellite, and found evidence for enhanced electric-field waves, in addition to perturbations in electron density and temperature associated with NWC, around a large area situated 400 km north of NWC. The authors likewise connect the enhanced electric-field waves to transmitter-induced plasma irregularities.

While the evidence for VLF spectral broadening associated with the NWC transmitter are thoroughly documented, a characterization of the NWC-induced plasma density fluctuations is absent. Furthermore, most studies so far were based on heliosynchronous satellites such as DEMETER and ZH-1, which can cover only two local time sectors 12-hour apart. We analyze 456 conjunctions between the Swarm A and B satellites and NWC, and 58 conjunctions between NorSat-1 and NWC. Through high frequency plasma density observations (16 Hz sampling frequency from the Swarm Advanced Plasma Density dataset, and 1000 Hz sampling frequency using the m-NLP instrument aboard NorSat-1), we present a scale-dependent characterization and climatology of strong plasma fluctuations induced by the NWC transmitter, with a seamless local time coverage. Further, we discuss whether the NWC transmitter is inducing turbulent plasma irregularities in the topside F-region, based on both magnetic field fluctuations and satellite scintillations measured by Swarm.

2 Methodology

Central to the analysis used in the present study is the power spectral density (PSD) of a signal consisting of in-situ measured plasma density. As the PSD of a signal reflects the intensity at which the signal fluctuates at a given frequency, a PSD analysis is particularly useful to study the scale-dependency of ionospheric plasma phenomena. In this study, we subject data from the Swarm mission and novel data from the NorSat-1 satellite to a PSD analysis.

The Swarm satellites have been orbiting Earth in polar orbits since late 2013 (Friis-Christensen et al., 2006), at an altitude between 450 km and 520 km. Consisting of three

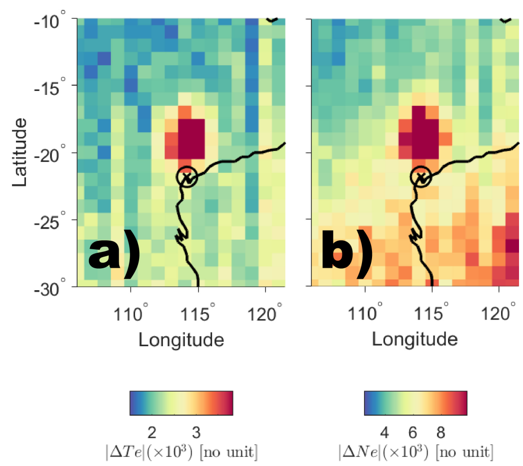

Figure 1. The ionospheric "hotspot" associated with NWC, based on data from the Langmuir probe aboard Swarm A and B, calculated using median values from 5146 passes over the an extended area around NWC by Swarm A and B, made during local magnetic times between 21 h and 6 h, for the entire Swarm mission period. Panel a) shows the absolute value of ΔT, while panel b) shows the absolute value of Δn, quantities to be defined in the text. The NWC transmitter is marked with a circle and a cross.

identical satellites, A, B, and C, the mission entails measurements of Earth's near space environment using an array of instruments. Among these, we mainly use data from the Thermal Ion Imager instrument, covering the entire mission period from 2014 through 2020. In particular, the Swarm Advanced Plasma Density dataset consists of 16 Hz resolution observations made from measuring faceplate currents (Knudsen et al., 2017).

The NorSat-1 satellite is a multi-payload micro-satellite, and Norway's first scientific satellite, launched in 2017. NorSat-1 is equipped with the multi-Needle Langmuir Probe system (m-NLP) (Jacobsen et al., 2010; Bekkeng et al., 2010), which gives plasma density observations with a sampling frequency of 1000 Hz, and which has successfully flown on several sounding rockets in the polar ionosphere (see, e.g., Lynch et al., 2015; Spicher et al., 2016). NorSat-1 orbits earth at an altitude of 600 km in a stable quasi-heliosynchronous orbit, meaning NorSat-1 consistently crosses the equator heading north at a local time of around 23 h on Earth's nightside. In the present study, we will only use data from one cylindrical Langmuir probe, which on NorSat-1 has a radius much smaller than typical topside F-region ionosphere plasma Debye lengths. The probe has a fixed positive bias with respect to the plasma potential, leading to the probe attracting electrons from the surrounding plasma. Changes in the number of attracted electrons will then reflect fluctuations in the surrounding plasma density and temperature. The data from NorSat-1 stem from 2017 through 2020, though there are large gaps in the data. Coincidentally, plasma observations from NorSat-1 has recently been utilized to investigate electron heating by very high frequency radio transmitter (Chernyshov et al., 2020).

For both datasets, we are interested in plasma fluctuations irrespective of the background density, and so we construct the dimensionless relative density fluctuations Δn,

$$\Delta n = \frac{n - \bar{n}_{1m}}{\bar{n}_{1m}}, \tag{1}$$

where n_{1m} is a running median filter with a window size of 1 minute. In the case of NorSat-1 data, we take the probe current I as a placeholder for n. That is, for NorSat-1,

$$\Delta n = \frac{I - \bar{I}_{1m}}{\bar{I}_{1m}}. \tag{2}$$

Next, we subject the relative density fluctuations to a PSD density analysis, where we use a variant of Welch's power spectral density (Welch, 1967). This method entails averaging modified periodograms over fixed logarithmically spaced spectral range (Tröbs & Heinzel, 2006). The resulting power spectrum, $S(f)$ is a scale-dependent quantity that measures the strength of fluctuations in the observed plasma density at a given frequency f, which corresponds to a spatial scale λ,

$$\lambda = \frac{v_S}{f}, \tag{3}$$

v_S being spacecraft orbital velocity, assuming that the latter is much greater than the local plasma velocity. As the satellites are moving at around 7.6 km/s with respect to Earth, this assumption is reasonable [see Fredricks and Coroniti (1976) for a comprehensive discussion on the relation between the true spectrum and one obtained by means of a moving spacecraft]. Note that the unit for $S(\lambda)$ here is Hz^{-1}, as the quantities we are subjecting to a PSD analysis are unitless. We finally also note that similar, albeit noisier, results can be obtained by averaging or interpolating a conventional fast Fourier transform spectrum instead of performing the aforementioned PSD analysis.

We divide the Δn data into bins of size of 60 seconds, and space these bins out with a temporal resolution of 1 second, meaning the bins have 98% overlap. Then, we calcu-

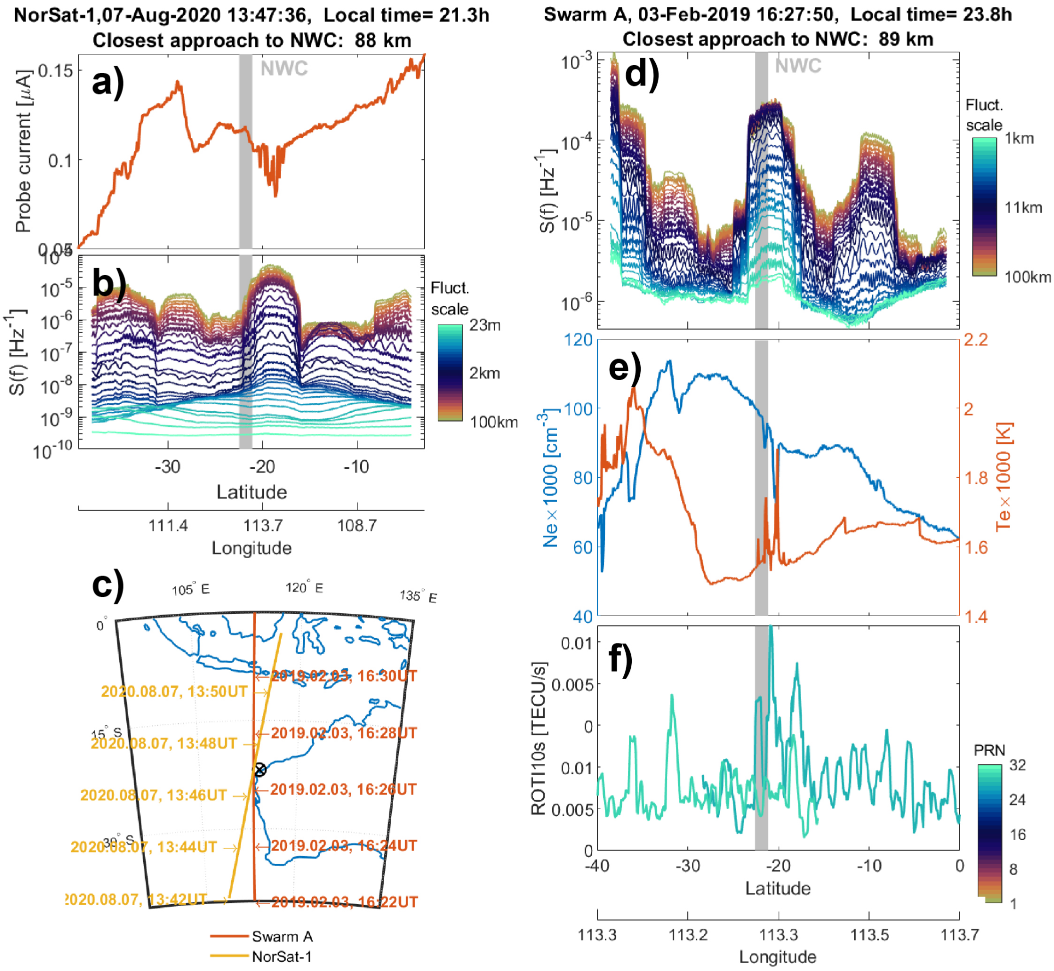

Figure 2. **Panels a) and b):** A pass made by NorSat-1 over NWC on 7 August 2020, at a local time of 21.3 h (the path traversed by Swarm A is shown in panel c). Panel a) shows the current through the m-NLP probe carrying the highest bias (10 V with respect to the spacecraft potential). Panel b) panel shows $S(\lambda)$ of the relative density fluctuations for 32 scales, from 100 km down to 23 m, indicated by the colorbar. The latitudes and longitudes of this pass over NWC are indicated along the two bottom x-axes.
Panels d), e) and f): A pass made by Swarm A over NWC on 3 February 2019, at a local time of 23.8 h (the path traversed by NorSat-1 is shown in panel c). Panel a) shows $S(\lambda)$ for 32 scales, from 100 km down to 1 km, indicated by the colorbar. Panel d) shows electron density (left axis) and temperature (right axis). Panel e) shows ROTI from all visible PRN with an elevation angle greater than 30°, with PRN number indicated by the colorbar. The latitudes and longitudes of this pass over NWC are indicated along the two bottom x-axes, and in all five panels, the geographic location of NWC is indicated by a gray shaded line.

late $S(\lambda)$ for 32 logarithmically spaced scales ranging from 100 km down to the smallest scale available. The smallest scale for the Swarm 16 Hz data is 1 km, and 23m for the NorSat-1 1000 Hz data. Note that 23 m is larger than the scale corresponding to the NorSat-1 Nyquist frequency of 500 Hz. This is due to an electronic filter, which reduces the highest frequency for which the spectrum contains valuable information to 333 Hz.

In addition to the PSD analysis, we use plasma observations from the Swarm Langmuir probe and the Vector Field Magnetometer, and data from the Swarm GPS receivers. From the Langmuir probe data, we gather 2 Hz electron density and temperature, while we gather 50 Hz magnetic field fluctuations from the Vector Field Magnetometer. Here, we follow Park, Lühr, Knudsen, et al. (2017) in transforming the magnetic field fluctuations into the mean-field aligned (MFA) coordinate system, allowing us to scrutinize fluctuations in the field-perpendicular component; this corresponds to fluctuations in the local field aligned currents (FAC). From the Swarm GPS data, we follow Jin et al. (2019) in calculating the 1 Hz TEC (Total Electron Content), from which we estimate the rate of change of TEC index (ROTI), where we take the standard deviation of the rate of change TEC in a 10 second window. ROTI can, under certain circumstances, reflect the amount of satellite scintillations in the GPS signal between the Swarm satellite and the up to 8 GPS satellites that are tracked by each Swarm satellite.

In Fig. 1, we show the median values of $|\Delta n|$ (panel a) and $|\Delta T|$ (panel b), where ΔT is similarly defined as Δn, for the electron temperature T. Note that as both quantities fluctuate around 0, and so we consider the absolute value in Fig. 1, and the numbers are multiplied by a factor of 10^3 for ease of reading. The median values are based on 5146 passes made by Swarm A and B over an extended area around NWC, where the location of NWC is indicated with a cross and a circle. The ionospheric "hotspot" associated with NWC clearly appears north of NWC's geographic location, where there is a significant enhancement in both $|\Delta n|$ and $|\Delta T|$.

In Fig. 2, we show a conjuction between NorSat-1 and NWC (panels a and b), and between Swarm A and NWC (panels d, e, and f). The two orbital paths are displayed in panel c), where we bring attention to the fact that the two conjunctions displayed occurred 18 months apart, but are shown in the same figure for illustration purposes. Panel a) shows the current through one m-NLP probe, and panel b) shows the resulting $S(\lambda)$ for the 32 scales indicated by the colorbar. Panel d) shows the Swarm A-calculated $S(\lambda)$, for 32 scales indicated by the colorbar. Panel e) shows the 2 Hz electron temperature (right axis) and density (left axis). Lastly, panel f) shows the ROTI for GPS satellites with an elevation angle greater than 50°, with PRN number indicated by the colorbar. The satellite's orbital path is indicated by latitude and longitude on the two bottom x-axes. The geographic location of NWC is indicated by a shaded gray line in each panel (and with a circle and a cross in panel c). We see that northward of NWC, there is a dip in both the probe current (panel a) and electron density (panel d), and a corresponding perturbation to the electron temperature (panel d). In the $S(\lambda)$ panels (b and c), we see that there is a distinctive feature in $S(\lambda)$ northward of NWC: Some scales increase sharply, while other scales do not change noticeably after the satellite passes NWC, indicating a scale-dependent response in the plasma density to the NWC VLF transmitter.

3 Results

We analyze 456 conjunctions between Swarm A and B, and NWC, where we define a conjuction as a pass by the satellite over NWC with a maximum distance of 150 km between the projected location of the satellite on Earth's surface and the geographic location of NWC. The reason for not including conjunctions made by Swarm C is that Swarm C follows the orbit of Swarm A closely, with only a short longitudinal distance. Including Swarm C would thus risk double-counting events. We perform a superposed epoch analysis on all passes made by the satellites over NWC. By taking the median of several

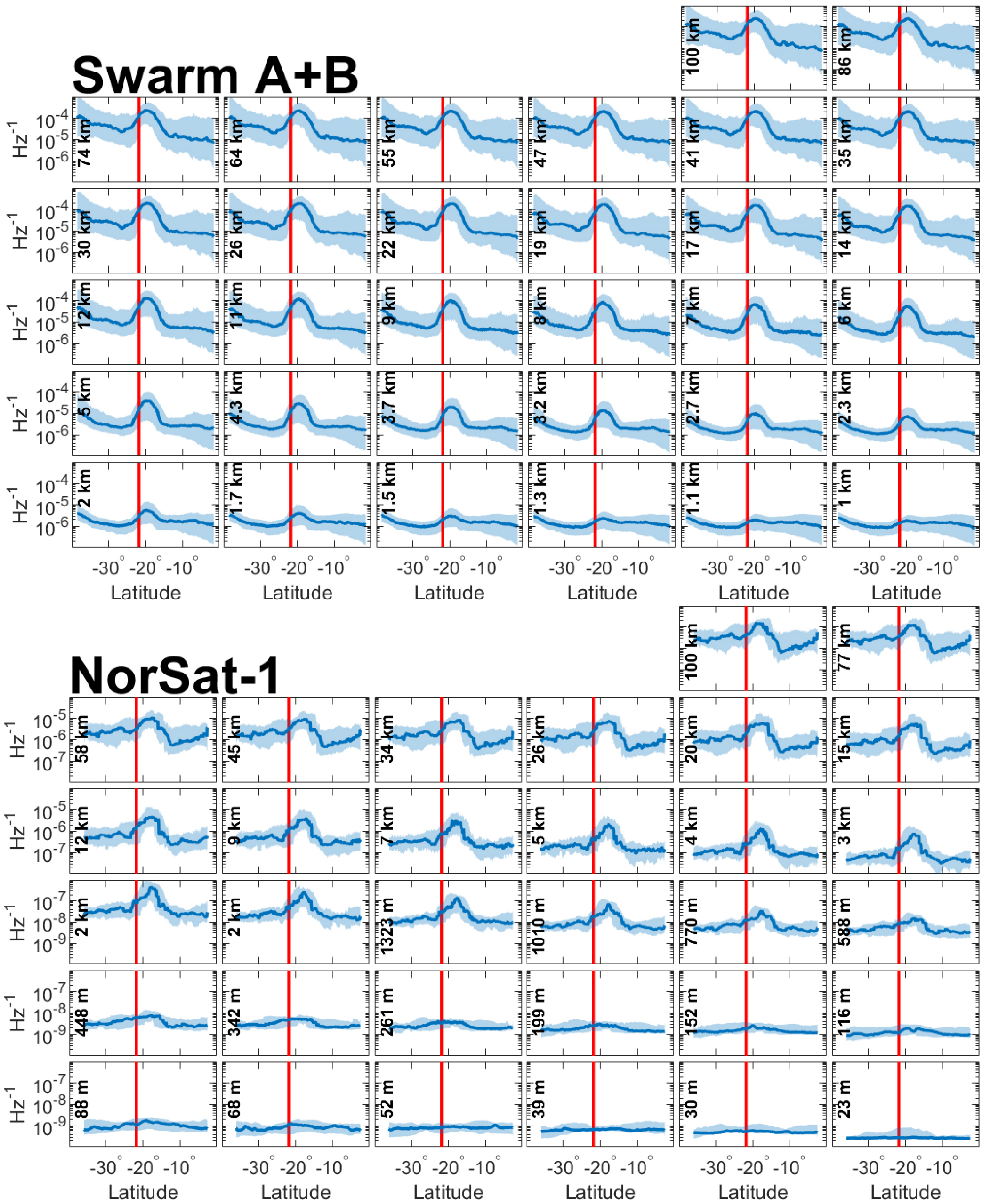

Figure 3. Plasma density fluctuations, $S(\lambda)$, in a superposed epoch analysis of 173 passes made by Swarm A+B (top) and 27 passes made by NorSat-1 (bottom), directly over NWC (maximum distance of 150 km within NWC). The Swarm passes are made during magnetic local times between 21 h and 6 h, while all NorSat-1 passes occurred at local times between 21 h and 23 h. For each panel, the relevant scale interval is indicated. Note that for the NorSat-1 panels, the limits along the y axes are different for the lower 18 scales, though for all 64 panels, the limits range over four orders of magnitude.

orbits in superposition, after shifting southward-bound orbits northward, we can eliminate the effect of local plasma conditions encountered before and after NWC. In Fig. 3, we present a superposed epoch analysis of 173 passes made by Swarm A and B (top 32 panels) during magnetic local times between 21 h and 6 h, and 27 passes made by NorSat-1 (bottom 32 panels), during magnetic local times between 21 h and 23 h. Each panel show the superposition of $S(\lambda)$ for a scale interval given by its midpoint, inset on the left axis. Each of of the 200 conjunctions with NWC upon which Fig. 3 is based are included in the Supporting Information to this article, as plots akin to those shown in Fig. 2.

We can clearly see that there is a peak in $S(\lambda)$ north of NWC, and that the prominence of the peak varies depending on the scale interval at which $S(\lambda)$ is calculated; while prominent in some panels, the peak is almost invisible in others. This could indicate that power is being injected into the density fluctuation signal at certain scales. To quantify this scale-dependency, we perform a peak prominence analysis to each scale interval. We define prominence p as,

$$p_\lambda = \frac{\sigma_{\lambda,\mathrm{max}}}{\sigma_{\lambda,\mathrm{base}}} - 1, \tag{4}$$

where $\sigma_{\lambda,\mathrm{max}}$ is the maximum peak fluctuation power associated with NWC, and $\sigma_{\lambda,\mathrm{base}}$ is the median fluctuation power before and after NWC, both calculated after smoothing $S(\lambda)$, to avoid giving significance to local minima and maxima. In this context, we interpret the prominence p_λ as the excess power contained in the plasma fluctuations at the scale λ, where $p_\lambda = 0$ would indicate that no excess power is associated with the NWC at that particular scale. The distribution of p_λ across λ generally exhibit a prominent peak at lower scales, but remains high across a large range of scales. To measure the location of the peak, which corresponds to the scale at which we observe maximum excess density fluctuations, we fit a two-term Gaussian curve,

$$p_{\mathrm{fit}}(\lambda) = p_a \exp\left[-\left(\frac{\lambda-\lambda_0}{\lambda_a}\right)^2\right] + p_b \exp\left[-\left(\frac{\lambda-\lambda_1}{\lambda_b}\right)^2\right], \tag{5}$$

where $p_{a,b}$, $\lambda_{0,1}$ and $\lambda_{a,b}$ are fitting parameters determined by the fitting algorithm. Crucially, λ_0 represents the location of the peak in the prominence distribution. Now, in choosing the specific function to fit to the prominence data, the goal is to isolate λ_0, the overall peak in the distribution. The choice of a two-term Gaussian is somewhat arbitrary, and similar results could be had by applying different functions. We will therefore not interpret the role of the other fitting parameters.

As mentoned, in the context of power being injected into the plasma density fluctuation PSD, λ_0 is the scale at which we observe maximum excess density fluctuations associated with the NWC transmitter. Indeed, the end product of this analysis is λ_0, and to quantify the uncertainty associated with this analysis, we perform a Boostrap error analysis with 10^4 iterations. In each iteration, orbits passing over NWC are re-sampled uniformly with replacement. We then use the 90-percent confidence intervals of all iterations as errorbars for our estimate of λ_0

In Fig. 4, we show the result of this statistical analysis applied to all conjunctions between Swarm A, B and NorSat-1, and NWC.

Panel a) shows an analysis based on magnetic local time. Here, we see the p_λ distribution for passes made by Swarm A and B, during noon ($9 < \mathrm{MLT} < 15$), dusk ($15 < \mathrm{MLT} < 21$), dawn ($3 < \mathrm{MLT} < 9$), and midnight ($21 < \mathrm{MLT} < 3$), where we use the altitude adjusted corrected geomagnetic coordinates system for MLT-calculations (Baker & Wing, 1989). While completely absent during noon and dusk, the excess power in the density signal associated with NWC remains comparatively low for dawn passes, but is in excess of 15 times higher for passes made during magnetic midnight. The small-scale (< 10 km) fluctuations associated with the NWC peak is strongly suppressed in the dawn distribution, where there is great uncertainty in the location of λ_0, while the peak for the midnight distribution is located at the scale $\lambda_0 = 6.7 \pm 1.7$ km. In panel a), and the subsequent three panels, the shaded area behind the two-term Gauss curve are fits made from the upper and lower quartile p_λ distributions from all the 10^4 Bootstrap iterations.

In Panel b), we analyze the effect of geomagnetic activity on the NWC-associated density fluctuations, where we only include passes made during 21 h $<$ MLT $<$ 6 h, the MLT interval in which the strongest excess fluctuations are visible. Here, we use the SYM-H index (Wanliss & Showalter, 2006), provided by OMNI (King & Papitashvili, 2005), as a measure of the geomagnetic activity affecting the mid-latitude ionosphere. Quiet times are defined as passes made during times with an average value of SYM-H > -15 nT, while active times are defined as the opposite. We see that the excess plasma density fluctuations associated with NWC are around 15 times stronger during quiet geomagnetic times, compared to around 10 times stronger during active times. The peak scale for the excess plasma density fluctuations remain similar across geomagnetic activity, with $\lambda_0 = 7.1 \pm 1.1$ km for passes made during geomagnetically quiet times, and $\lambda_0 = 7.9 \pm 2.9$ km for passes made during active times.

In panel c) of Fig. 4, we show the prominence analysis for three different seasons, where we again only include passes made during MLTs between 21 h and 6 h. Here, we define June and December solstices as a 90-day period centered on each solstice, while we combine the equinoxes, in which a 90-day period is centered on the Spring and Autumn equinoxes respectively. We observe that the December solstice passes barely register a prominent peak associated with NWC for any scale, while the June solstice passes measure fluctuations barely 10 times stronger associated with NWC, with a peak at $\lambda_0 = 5.5 \pm 1.0$ km. However, the combined Equinox passes measure excess plasma fluctuations at NWC 25 times stronger than before and after NWC, with a peak in the prominence distribution at $\lambda_0 = 7.7 \pm 1.6$ km.

In panel d), we divide all Swarm A and B conjunctions into three periods, Early (from 2014 - June 2016), Mid (June 2016 - September 2017), and Late (September 2017 - January 2021). As dictated by Swarm orbital dynamics, each period contains roughly the same number of passes, despite being of varying length. During the Early period, the solar cycle is descending from a maximum, a descent that continues through the Mid period. As the Late period progresses, the deep solar minimum has begun. The resulting prominence stays around 10 for the Early ($\lambda_0 = 8.5 \pm 3.7$ km) and Mid ($\lambda_0 = 4.6 \pm 1.2$ km) periods, with the Mid period small-scale fluctuations more pronounced. However, the Late period exhibits considerably more fluctuations associated with NWC, with prominence reaching 20. The latter exhibits a peak at $\lambda_0 = 6.7 \pm 1.5$ km.

Finally, in panel e), we show how each satellite differs in the way the NWC-induced plasma density fluctuations are measured, where we now only include passes made during magnetid midnight (21 h $<$ MLT $<$ 3 h), which is the only MLT interval in which NorSat-1 crosses the nightside ionosphere. We see that Swarm A and B show a very similar distribution in p_λ, with peaks located at $\lambda_0 = 6.0 \pm 2.3$ km and $\lambda_0 = 6.9 \pm 1.9$ km respectively, despite Swarm A orbiting at an altitude of around 450 km, while Swarm B orbits at an altitude around 500 km. The NorSat-1 distribution, however, is different, with a peak located at $\lambda_0 = 2.8 \pm 1.1$ km, and with excess NWC-associated plasma density fluctuations existing on scales down to around 100 m (see Fig. 3 for the superposed epoch analysis on which the NorSat-1 datapoints in panel d of Fig. 4 are based). While the Swarm A and B passes register excess plasma density fluctuations around 15 times stronger over NWC, NorSat-1 registers fluctuations only around 8 times stronger.

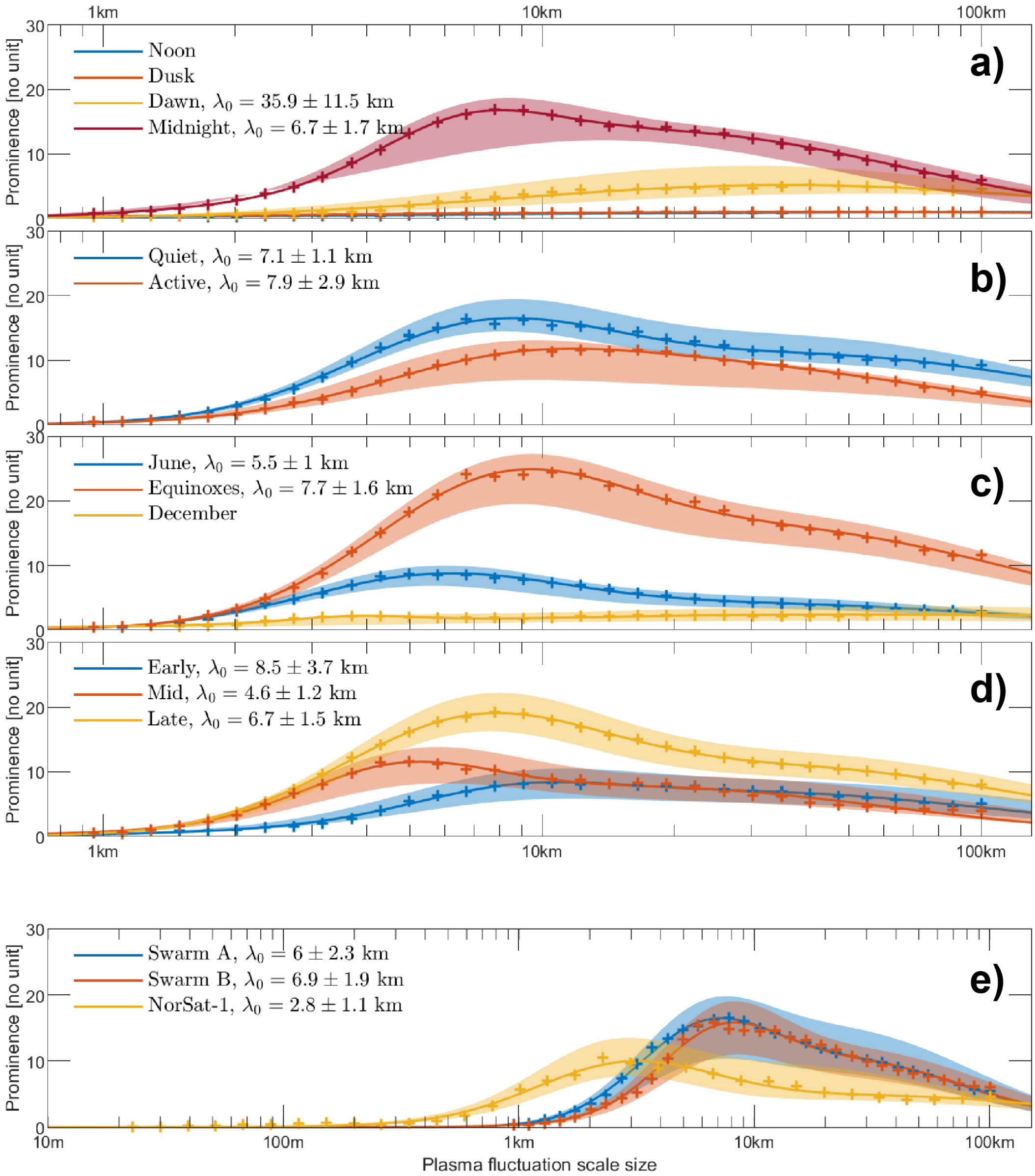

Figure 4. **Panel a)** shows the prominence analysis based on orbits made by Swarm A and B, during four different MLT intervals, noon (9h < MLT < 15h), dusk (15h < MLT < 21h), dawn (3 < MLT < 9), and midnight (21h < MLT <3h). **Panels b), c), and d)** likewise show the analysis based on orbits made by Swarm A and B, but for an MLT interval of 21h < MLT < 6h. In **Panel b)** The data is divided into quiet (SYM-H > -15 nT) and active (SYM-H < -15 nT) geomagnetic conditions. **Panel c)** shows the corresponding analysis for three seasons, June and December solstices, along with combined equinoxes. **Panel d)** divides the data into three periods, Early (from 2014 - June 2016), Mid (June 2016 - September 2017), and Late (September 2017 - January 2021). **Panel e)** compares the analysis based on Swarm A, Swarm B and NorSat-1, where the Swarm passes over NWC were made bwteen 21h < MLT < 3h, and the NorSat-1 passes between 21h < MLT < 23 h. In each panel a two-term Gaussian curve is fitted through the prominence datapoints [Eq. (5)]. The error intervals for λ_0 are 90-percent confidence intervals from a Bootstrap error analysis, and the shaded area behind each fitted curve are fits corresponding to the upper and lower quartile distributions of the data. The Bootstrap analysis consists of 10^4 iterations of the original data, with uniform resampling of the orbits — this represents the statistical uncertainty in the underlying data.

4 Discussion

The overall distribution of excess NWC-associated plasma density fluctuations as seen by NorSat-1 (Fig. 4, panel d) differs from that of Swarm A and B. The reasons for this is many-faceted. Firstly, NorSat-1 consistently crosses the nightside equator at MLTs between 21 h and 23 h, while the nightside Swarm A and B crossings are not confined in MLT. Furthermore, NorSat-1 orbits at the considerably higher altitude of 600 km. However, since the 50 km that separates Swarm A from Swarm B in altitude has little impact on their p_λ distributions, the altitude difference between NorSat-1 and the Swarm satellites would similarly not contribute to the observed distribution difference. Finally, the sharp cutoff of the Swarm A and B p_λ distributions around $\lambda = 1$ km is close to the Nyquist frequency of the 16 Hz Swarm Advanced Plasma Density sampling frequency (8 Hz). We then expect the true distribution of excess NWC-associated plasma density fluctuations to be closer to that seen by NorSat-1, since the latter can unhindered investigate scales smaller than 1 km, and indeed down to 23 m.

The climatology of the NWC-associated plasma fluctuations show that the fluctuations are strongest during magnetic midnight, and partially during dawn, when the ambient plasma density is low. This harmonizes with findings that VLF spectral broadening over NWC favours conditions with low ambient plasma density (Xia et al., 2020), and with recent reports that a low ambient plasma density creates conditions favourable to the transmission of man-made electromagnetic waves (Parrot, 2021).

At first glance, it might seem counter-intuitive that the combined equinoxes-passes exhibit considerably more prominent NWC-associated plasma fluctuations than the solstice passes (panel c). After all, the midnight ionosphere near Australia is denser during equinoxes than during the June solstice (Jee et al., 2009). However, at the same time, the nighttime ionosphere around Australia is inherently disturbed by irregularities during both solstices, and especially during the June solstice (Kil & Paxton, 2017). This indicates that tenuous undisturbed plasma creates favourable conditions for the NWC-associated plasma fluctuations, and explains the particularly prominent Equinox-passes. Indeed, as is readily seen in panel b), prominent fluctuations are favoured during times when the ionosphere is geomagnetically quiet, as opposed to active.

Dividing all the conjunctions into three periods (panel d) drives the point home. The NWC-associated plasma fluctuations are weakest in the Early period, before getting successively more pronounced until the Late period. The latter contains the current deep solar minimum, indicating a reverse proportionality between NWC-associated plasma fluctuations and solar activity. The entire climatology thus indicates that the conditions most favourable to NWC-associated plasma fluctuations involve a low-density, tenuous ionosphere, with a preference for low solar activity.

It is now prudent to take a step back, and briefly take into account the difference between plasma *fluctuations* and plasma *irregularities*: Whereas the former is inherently stable, irregularities arise from an instability mechanism. Although far from perfectly understood, instability mechanisms enable an initial equilibrium state to become unstable to perturbation, ultimately leading to turbulence (Huba et al., 1985; Fasoli et al., 2006). In this context, spectral broadening of VLF radio signals is known to be caused by both large- and small-scale ($\sim$ 100 m) ionospheric plasma irregularities (Groves et al., 1988; Rozhnoi et al., 2008; Rapoport et al., 2010). In fact, the presence of VLF broadening can be seen as a footprint of plasma turbulence in the topside ionosphere (Titova et al., 1984). Moreover, spectral broadening of VLF signals has recently been observed and characterized at an altitude of 600 km over NWC (Mishin et al., 2010; Xia et al., 2020). The authors of these studies posited that the observed spectral broadening was due to scattering by turbulent plasma instabilities caused by the VLF signal itself.

As we have shown evidence of strong excess plasma fluctuations consistently being observed in the topside F-region ionosphere above NWC, it is tempting, in light of the observed VLF spectral broadening, to conclude that the NWC signal transmitter is producing turbulent plasma structuring.

However, when subjecting the Swarm TEC data to the same superposed epoch analysis as described in the previous section, we find no evidence that the plasma fluctuations are consistently inducing changes in the measured TEC. Fig. 5 shows a superposed epoch analysis based on passes made by Swarm A and B during 21 h $<$ MLT $<$ 6 h, and during geomagnetically quiet conditions (SYM-H> -15 nT). In panel a), we plot the median $S(\lambda)$ for all 124 identified passes, which clearly shows the scale-dependent response to NWC in the plasma density data. In panel b), we show a similar treatment to the field-perpendicular magnetic field fluctuations: We show the superposed epoch analysis of $S(\lambda)$ for 32 scales from 100 km down to 305 m, where we subjected the magnetic field data to a PSD analysis similar to that presented in the Methodology section. (Note that the magnetic field fluctuations are not unitless like the density data.) In panel c) we show all the ROTI observations calculated from the GPS receivers onboard Swarm A and B (elevation angle greater than 50°), during the 124 passes mentioned, with the median of all passes displayed in red. As is readily observed, the ROTI data does not exhibit any clear pattern associated with NWC, apart from circumstantial evidence from individual passes (which is also evident in Fig. 2, panel f).

Now, FAC structuring is directly associated with equatorial plasma irregularities [Farley (1963); Stolle et al. (2006), Figs 2, 11, and 12; Rodríguez-Zuluaga et al. (2017), Figs 1, 2, and 4; Rodríguez-Zuluaga and Stolle (2019), Figs 1 and 2]. In panel b) of Fig. 5, the magnetic field fluctuations show no clear response to NWC, meaning that there are no FAC structuring associated with NWC, and that background FACs are not consistently being disturbed by the VLF signal. Furthermore, the ROTI data from the Swarm GPS receivers are known to correlate with the occurrence of plasma irregularities (Jin et al., 2019). That we observe no enhancements in ROTI over NWC could indicate that there are no more plasma irregularities present over NWC than in the immediate vicinity. As such, we believe it is premature to conclude that the NWC VLF signal is producing turbulent structuring of the topside F-region ionosphere.

As a counterpoint, we are consistently observing strong plasma fluctuations associated with NWC, using three different instruments: The Langmuir probes and Thermal Ion Imager onboard Swarm, and the m-NLP instrument onboard NorSat-1. The wavelength of the 19.8 kHz signal (15 km) from the NWC transmitter matches scales on which we observe strong plasma fluctuations. Likewise, plasma irregularities could conceivably exist without corresponding FAC structuring, depending on local conditions. And while rapid changes in TEC as calculated using the Swarm GPS receivers could correspond to satellite scintillations, the 1 Hz frequency with which the data is supplied could make it unsuitable for detecting scintillations (Park, Lühr, Kervalishvili, et al., 2017). In addition, to the authors' best knowledge, there are no acceptable ways to calculate the precise position of the ionospheric piercing point between Swarm and the GPS satellites. Any scintillations observed in-situ using the Swarm GPS receivers could then originate from locations far removed from the Swarm satellite, which could make the Swarm GPS data unsuitable for highly localized phenomena such as the one we are dealing with in the present study. To compound the situation, to the authors' best knowledge, there are no suitable ground-based instruments capable of observing scintillations around NWC. In summary, we believe further investigation into the link between the NWC transmitter and topside F-region plasma irregularities is necessary.

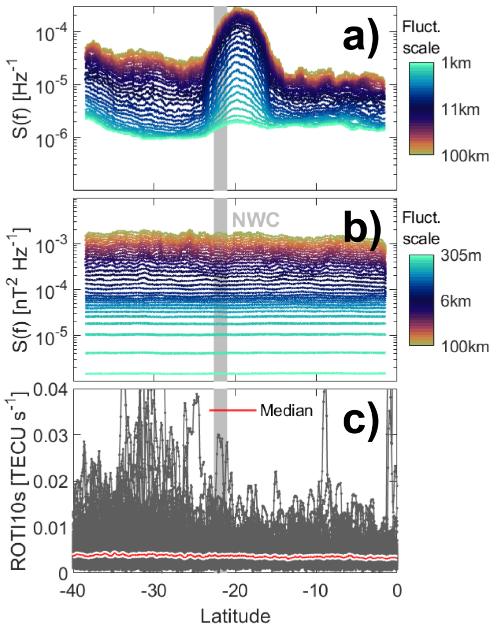

Figure 5. The superposed epoch analysis based on passes made by Swarm A and B during 21 h < MLT < 6 h. Panel a) displays the median $S(\lambda)$ for all 32 scales, with scale given by the colorbar. Similarly, panel b) shows the corresponding $S(\lambda)$ for the field-perpendicular magnetic field fluctuations, calculated using the Swarm 50 Hz magnetic field data, and where we use the meridional magnetic field component. Panel c) shows ROTI for all available GPS satellites with an elevation angle greater than 50°, for the same passes that constitute the superposed epoch analyses in panels a) and b), where the median ROTI is displayed with a red line.

5 Conclusion

We analyze in total 514 conjunctions between satellites orbiting in the topside F-region ionosphere, and the NWC VLF signal transmitter. This gives us a rich database of in-situ plasma measurements from Swarm A and B with a seamless local time, along with novel data from NorSat-1, a satellite carrying an instrument capable of sampling plasma density with a sampling frequency of 1000 Hz. We subject plasma density observations from all three satellites to a PSD analysis, and a consequent superposed epoch analysis. We present a detailed account of the scale-dependency of the plasma fluctuations associated with NWC, in addition to a comprehensive climatology, documenting the conditions favourable NWC-associated plasma fluctuations.

While the result constitutes circumstantial evidence for the VLF signal transmitter-induced plasma irregularities, we also observe counter-evidence for the existence of irregularities induced by NWC. While not concluding that there are VLF signal-induced plasma irregularities in the topside F-region ionosphere above NWC, we have documented strong plasma fluctuations that clearly originate from the NWC signal. If absent of turbulent structuring, these plasma fluctuations could be smooth, regular waves with wavelengths larger than 1 km - 10 km. These findings should be seen in a wider context, in that they complement the link between VLF spectral broadening and turbulence in the topside ionosphere.

Acknowledgments

This work is a part of the 4DSpace initiative at the University of Oslo, and is supported in part by Research Council of Norway grants 275655, 275653 and 267408. The authors acknowledge ESA for the provision of the Swarm data, which was accessed from `https://earth.esa.int/web/guest/swarm/data-access`, and acknowledge NASA/GSFC for the Space Physics Data Facility's OMNIWeb service. The NorSat-1 data used in this tudy can be accessed from `some_https_url`. The authors would like to extend thanks to D. J. Knudsen, J. K. Burchill, and S. C. Buchert for their work on the Swarm Thermal ion imager instrument, and extend thanks to the NorSat-1 team at the University of Oslo.

References

Baker, K. B., & Wing, S. (1989, July). A new magnetic coordinate system for conjugate studies at high latitudes. *Journal of Geophysical Research: Space Physics*, *94*(A7), 9139–9143. Retrieved 2018-03-07, from `http://onlinelibrary.wiley.com/doi/10.1029/JA094iA07p09139/abstract` doi: 10.1029/JA094iA07p09139

Bekkeng, T. A., Jacobsen, K. S., Bekkeng, J. K., Pedersen, A., Lindem, T., Lebreton, J.-P., & Moen, J. I. (2010). Design of a multi-needle Langmuir probe system. *Measurement Science and Technology*, *21*(8), 085903. Retrieved 2018-06-11, from `http://stacks.iop.org/0957-0233/21/i=8/a=085903` doi: 10.1088/0957-0233/21/8/085903

Chernyshov, A. A., Chugunin, D. V., Frolov, V. L., Clausen, L. B. N., Miloch, W. J., & Mogilevsky, M. M. (2020). In Situ Observations of Ionospheric Heating Effects: First Results from a Joint SURA and NorSat-1 Experiment. *Geophysical Research Letters*, *47*(13), e2020GL088462. Retrieved 2021-01-23, from `https://agupubs.onlinelibrary.wiley.com/doi/abs/10.1029/2020GL088462` (_eprint: https://agupubs.onlinelibrary.wiley.com/doi/pdf/10.1029/2020GL088462) doi: https://doi.org/10.1029/2020GL088462

Chernyshov, A. A., Chugunin, D. V., Mogilevsky, M. M., Moiseenko, I. L., Ilyasov, A. A., Vovchenko, V. V., ... Korobkov, S. V. (2016, January). Approaches to studying the multiscale ionospheric structure using nanosatellites. *Geomag-*

netism and Aeronomy, *56*(1), 72–79. Retrieved 2021-01-25, from https://doi.org/10.1134/S0016793216010047 doi: 10.1134/S0016793216010047

Cohen, M. B., & Inan, U. S. (2012). Terrestrial VLF transmitter injection into the magnetosphere. *Journal of Geophysical Research: Space Physics*, *117*(A8). Retrieved 2021-01-25, from http://agupubs.pericles.prod.literatumonline.com/doi/abs/10.1029/2012JA017992 (_eprint: https://onlinelibrary.wiley.com/doi/pdf/10.1029/2012JA017992) doi: https://doi.org/10.1029/2012JA017992

Farley, D. T. (1963). A plasma instability resulting in field-aligned irregularities in the ionosphere. *Journal of Geophysical Research (1896-1977)*, *68*(22), 6083–6097. Retrieved 2021-01-29, from http://agupubs.onlinelibrary.wiley.com/doi/abs/10.1029/JZ068i022p06083 (_eprint: https://onlinelibrary.wiley.com/doi/pdf/10.1029/JZ068i022p06083) doi: https://doi.org/10.1029/JZ068i022p06083

Fasoli, A., Labit, B., McGrath, M., Müller, S. H., Plyushchev, G., Podestà, M., & Poli, F. M. (2006, May). Electrostatic turbulence and transport in a simple magnetized plasma. *Physics of Plasmas*, *13*(5), 055902. Retrieved 2021-02-02, from https://aip.scitation.org/doi/full/10.1063/1.2178773 (Publisher: American Institute of Physics) doi: 10.1063/1.2178773

Folkestad, K., Hagfors, T., & Westerlund, S. (1983). EISCAT: An updated description of technical characteristics and operational capabilities. *Radio Science*, *18*(6), 867–879. Retrieved 2021-01-25, from http://agupubs.onlinelibrary.wiley.com/doi/abs/10.1029/RS018i006p00867%4010.1002/%28ISSN%291944-799X.RADIOPROB1 (_eprint: https://onlinelibrary.wiley.com/doi/pdf/10.1029/RS018i006p00867) doi: https://doi.org/10.1029/RS018i006p00867

Fredricks, R. W., & Coroniti, F. V. (1976). Ambiguities in the deduction of rest frame fluctuation spectrums from spectrums computed in moving frames. *Journal of Geophysical Research (1896-1977)*, *81*(31), 5591–5595. Retrieved 2021-01-30, from http://agupubs.onlinelibrary.wiley.com/doi/abs/10.1029/JA081i031p05591 (_eprint: https://onlinelibrary.wiley.com/doi/pdf/10.1029/JA081i031p05591) doi: https://doi.org/10.1029/JA081i031p05591

Friis-Christensen, E., Lühr, H., & Hulot, G. (2006, April). Swarm: A constellation to study the Earth's magnetic field. *Earth, Planets and Space*, *58*, BF03351933. doi: 10.1186/BF03351933

Graf, K. L., Lehtinen, N. G., Spasojevic, M., Cohen, M. B., Marshall, R. A., & Inan, U. S. (2013). Analysis of experimentally validated trans-ionospheric attenuation estimates of VLF signals. *Journal of Geophysical Research: Space Physics*, *118*(5), 2708–2720. Retrieved 2021-01-25, from http://agupubs.onlinelibrary.wiley.com/doi/abs/10.1002/jgra.50228 (_eprint: https://onlinelibrary.wiley.com/doi/pdf/10.1002/jgra.50228) doi: https://doi.org/10.1002/jgra.50228

Groves, K. M., Lee, M. C., & Kuo, S. P. (1988). Spectral broadening of VLF radio signals traversing the ionosphere. *Journal of Geophysical Research: Space Physics*, *93*(A12), 14683–14687. Retrieved 2021-01-25, from http://agupubs.onlinelibrary.wiley.com/doi/abs/10.1029/JA093iA12p14683 (_eprint: https://onlinelibrary.wiley.com/doi/pdf/10.1029/JA093iA12p14683) doi: https://doi.org/10.1029/JA093iA12p14683

Huba, J. D., Hassam, A. B., Schwartz, I. B., & Keskinen, M. J. (1985). Ionospheric turbulence: Interchange instabilities and chaotic fluid behavior. *Geophysical Research Letters*, *12*(1), 65–68. Retrieved 2021-01-31, from http://agupubs.onlinelibrary.wiley.com/doi/abs/10.1029/GL012i001p00065 (_eprint: https://onlinelibrary.wiley.com/doi/pdf/10.1029/GL012i001p00065) doi: https://doi.org/10.1029/GL012i001p00065

Inan, U. S., Chang, H. C., & Helliwell, R. A. (1984). Electron precipitation zones around major ground-based VLF signal sources. *Journal of Geophysical Research: Space Physics*, *89*(A5), 2891–2906. Retrieved 2021-01-25, from http://agupubs.onlinelibrary.wiley.com/doi/abs/10.1029/JA089iA05p02891 (_eprint: https://onlinelibrary.wiley.com/doi/pdf/10.1029/JA089iA05p02891) doi: https://doi.org/10.1029/JA089iA05p02891

Jacobsen, K. S., Pedersen, A., Moen, J. I., & Bekkeng, T. A. (2010). A new Langmuir probe concept for rapid sampling of space plasma electron density. *Measurement Science and Technology*, *21*(8), 085902. Retrieved 2018-06-11, from http://stacks.iop.org/0957-0233/21/i=8/a=085902 doi: 10.1088/0957-0233/21/8/085902

Jee, G., Burns, A. G., Kim, Y.-H., & Wang, W. (2009). Seasonal and solar activity variations of the Weddell Sea Anomaly observed in the TOPEX total electron content measurements. *Journal of Geophysical Research: Space Physics*, *114*(A4). Retrieved 2021-02-01, from http://agupubs.onlinelibrary.wiley.com/doi/abs/10.1029/2008JA013801 (_eprint: https://onlinelibrary.wiley.com/doi/pdf/10.1029/2008JA013801) doi: https://doi.org/10.1029/2008JA013801

Jin, Y., Moen, J. I., Oksavik, K., Spicher, A., Clausen, L. B. N., & Miloch, W. J. (2017). GPS scintillations associated with cusp dynamics and polar cap patches. *Journal of Space Weather and Space Climate*, *7*, A23. Retrieved 2018-09-14, from https://www.swsc-journal.org/articles/swsc/abs/2017/01/swsc170040/swsc170040.html doi: 10.1051/swsc/2017022

Jin, Y., Spicher, A., Xiong, C., Clausen, L. B. N., Kervalishvili, G., Stolle, C., & Miloch, W. J. (2019). Ionospheric Plasma Irregularities Characterized by the Swarm Satellites: Statistics at High Latitudes. *Journal of Geophysical Research: Space Physics*, *124*(2), 1262–1282. Retrieved 2020-01-20, from https://agupubs.onlinelibrary.wiley.com/doi/abs/10.1029/2018JA026063 doi: 10.1029/2018JA026063

Kil, H., & Paxton, L. J. (2017). Global Distribution of Nighttime Medium-Scale Traveling Ionospheric Disturbances Seen by Swarm Satellites. *Geophysical Research Letters*, *44*(18), 9176–9182. Retrieved 2021-02-01, from http://agupubs.onlinelibrary.wiley.com/doi/abs/10.1002/2017GL074750 (_eprint: https://onlinelibrary.wiley.com/doi/pdf/10.1002/2017GL074750) doi: https://doi.org/10.1002/2017GL074750

King, J. H., & Papitashvili, N. E. (2005). Solar wind spatial scales in and comparisons of hourly Wind and ACE plasma and magnetic field data. *Journal of Geophysical Research: Space Physics*, *110*(A2). Retrieved 2020-07-16, from https://agupubs.onlinelibrary.wiley.com/doi/abs/10.1029/2004JA010649 (_eprint: https://agupubs.onlinelibrary.wiley.com/doi/pdf/10.1029/2004JA010649) doi: 10.1029/2004JA010649

Kintner P. M., Ledvina B. M., & de Paula E. R. (2007, September). GPS and ionospheric scintillations. *Space Weather*, *5*(9). Retrieved 2018-05-08, from https://agupubs.onlinelibrary.wiley.com/doi/10.1029/2006SW000260 doi: 10.1029/2006SW000260

Knudsen, D. J., Burchill, J. K., Buchert, S. C., Eriksson, A. I., Gill, R., Wahlund, J.-E., … Moffat, B. (2017, February). Thermal ion imagers and Langmuir probes in the Swarm electric field instruments. *Journal of Geophysical Research: Space Physics*, *122*(2), 2016JA022571. Retrieved 2018-03-07, from http://onlinelibrary.wiley.com/doi/10.1002/2016JA022571/abstract doi: 10.1002/2016JA022571

Leyser, T. (2001, August). Stimulated electromagnetic emissions by high-frequency electromagnetic pumping of the ionospheric plasma. *Space Science Reviews*, *98*(3), 223–328. Retrieved 2021-01-25, from https://doi.org/10.1023/A:1013875603938 doi: 10.1023/A:1013875603938

Leyser, T. B., & Wong, A. Y. (2009). Powerful electromagnetic waves for active environmental research in geospace. *Reviews of Geophysics*, *47*(1). Retrieved 2021-01-23, from http://agupubs.onlinelibrary.wiley.com/doi/abs/10.1029/2007RG000235 (_eprint: https://onlinelibrary.wiley.com/doi/pdf/10.1029/2007RG000235) doi: https://doi.org/10.1029/2007RG000235

Lynch, K. A., Hampton, D. L., Zettergren, M., Bekkeng, T. A., Conde, M., Fernandes, P. A., … Samara, M. (2015, November). MICA sounding rocket observations of conductivity-gradient-generated auroral ionospheric responses: Small-scale structure with large-scale drivers. *Journal of Geophysical Research: Space Physics*, *120*(11), 9661–9682. Retrieved 2018-08-15, from https://agupubs.onlinelibrary.wiley.com/doi/abs/10.1002/2014JA020860 doi: 10.1002/2014JA020860

Mishin, E. V., Starks, M. J., Ginet, G. P., & Quinn, R. A. (2010). Nonlinear VLF effects in the topside ionosphere. *Geophysical Research Letters*, *37*(4). Retrieved 2021-01-25, from http://agupubs.onlinelibrary.wiley.com/doi/abs/10.1029/2009GL042010 (_eprint: https://onlinelibrary.wiley.com/doi/pdf/10.1029/2009GL042010) doi: https://doi.org/10.1029/2009GL042010

Němec, F., Pekař, J., & Parrot, M. (2020). NWC Transmitter Effects on the Nightside Upper Ionosphere Observed by a Low-Altitude Satellite. *Journal of Geophysical Research: Space Physics*, *125*(12), e2020JA028660. Retrieved 2021-01-23, from https://agupubs.onlinelibrary.wiley.com/doi/abs/10.1029/2020JA028660 (_eprint: https://agupubs.onlinelibrary.wiley.com/doi/pdf/10.1029/2020JA028660) doi: https://doi.org/10.1029/2020JA028660

Park, J., Lühr, H., Kervalishvili, G., Rauberg, J., Stolle, C., Kwak, Y.-S., & Lee, W. K. (2017). Morphology of high-latitude plasma density perturbations as deduced from the total electron content measurements onboard the Swarm constellation. *Journal of Geophysical Research: Space Physics*, *122*(1), 1338–1359. Retrieved 2021-02-02, from http://agupubs.onlinelibrary.wiley.com/doi/abs/10.1002/2016JA023086 (_eprint: https://onlinelibrary.wiley.com/doi/pdf/10.1002/2016JA023086) doi: https://doi.org/10.1002/2016JA023086

Park, J., Lühr, H., Knudsen, D. J., Burchill, J. K., & Kwak, Y.-S. (2017). Alfvén waves in the auroral region, their Poynting flux, and reflection coefficient as estimated from Swarm observations. *Journal of Geophysical Research: Space Physics*, *122*(2), 2345–2360. Retrieved 2019-07-09, from https://agupubs.onlinelibrary.wiley.com/doi/abs/10.1002/2016JA023527 doi: 10.1002/2016JA023527

Parrot, M. (2021). Observations by DEMETER of man-made MF waves escaping from the ionosphere. *Journal of Geophysical Research: Space Physics*, *n/a*(n/a), 2020JA028954. Retrieved 2021-02-01, from http://agupubs.onlinelibrary.wiley.com/doi/abs/10.1029/2020JA028954 (_eprint: https://onlinelibrary.wiley.com/doi/pdf/10.1029/2020JA028954) doi: https://doi.org/10.1029/2020JA028954

Rapoport, V. O., Frolov, V. L., Polyakov, S. V., Komrakov, G. P., Ryzhov, N. A., Markov, G. A., … Rauch, J.-L. (2010). VLF electromagnetic field structures in ionosphere disturbed by Sura RF heating facility. *Journal of Geophysical Research: Space Physics*, *115*(A10). Retrieved 2021-01-25, from http://agupubs.onlinelibrary.wiley.com/doi/abs/10.1029/2010JA015484 (_eprint: https://onlinelibrary.wiley.com/doi/pdf/10.1029/2010JA015484) doi: https://doi.org/10.1029/2010JA015484

Rodríguez-Zuluaga, J., & Stolle, C. (2019, February). Interhemispheric field-aligned currents at the edges of equatorial plasma depletions. *Scientific Reports*, *9*(1), 1233. Retrieved 2021-02-01, from https://www.nature.com/articles/s41598-018-37955-z (Number: 1 Publisher: Nature Publishing Group) doi: 10.1038/s41598-018-37955-z

Rodríguez-Zuluaga, J., Stolle, C., & Park, J. (2017). On the direction of the Poynting flux associated with equatorial plasma depletions as derived from Swarm. *Geophysical Research Letters*, *44*(12), 5884–5891. Retrieved 2021-02-01, from http://agupubs.onlinelibrary.wiley.com/doi/abs/10.1002/2017GL073385 (_eprint: https://onlinelibrary.wiley.com/doi/pdf/10.1002/2017GL073385) doi: https://doi.org/10.1002/2017GL073385

Rozhnoi, A., Solovieva, M., Molchanov, O., Akentieva, O., Berthelier, J. J., Parrot, M., … Hayakawa, M. (2008, October). Statistical correlation of spectral broadening in VLF transmitter signal and low-frequency ionospheric turbulence from observation on DEMETER satellite. *Natural Hazards and Earth System Sciences*, *8*(5), 1105–1111. Retrieved 2021-01-26, from https://nhess.copernicus.org/articles/8/1105/2008/ (Publisher: Copernicus GmbH) doi: https://doi.org/10.5194/nhess-8-1105-2008

Spicher, A., Ilyasov, A. A., Miloch, W. J., Chernyshov, A. A., Clausen, L. B. N., Moen, J. I., … Saito, Y. (2016, October). Reverse flow events and small-scale effects in the cusp ionosphere. *Journal of Geophysical Research: Space Physics*, *121*(10), 10,466–10,480. Retrieved 2018-08-15, from https://agupubs.onlinelibrary.wiley.com/doi/abs/10.1002/2016JA022999 doi: 10.1002/2016JA022999

Stolle, C., Lühr, H., Rother, M., & Balasis, G. (2006). Magnetic signatures of equatorial spread F as observed by the CHAMP satellite. *Journal of Geophysical Research: Space Physics*, *111*(A2). Retrieved 2020-10-09, from https://agupubs.onlinelibrary.wiley.com/doi/abs/10.1029/2005JA011184 (_eprint: https://agupubs.onlinelibrary.wiley.com/doi/pdf/10.1029/2005JA011184) doi: 10.1029/2005JA011184

Streltsov, A. V., Berthelier, J.-J., Chernyshov, A. A., Frolov, V. L., Honary, F., Kosch, M. J., … Rietveld, M. T. (2018, October). Past, Present and Future of Active Radio Frequency Experiments in Space. *Space Science Reviews*, *214*(8), 118. Retrieved 2021-01-23, from https://doi.org/10.1007/s11214-018-0549-7 doi: 10.1007/s11214-018-0549-7

Stubbe, P., & HagforS, T. (1997, January). THE EARTH'S IONOSPHERE: A WALL-LESS PLASMA LABORATORY. *Surveys in Geophysics*, *18*(1), 57–127. Retrieved 2021-01-25, from https://doi.org/10.1023/A:1006583101811 doi: 10.1023/A:1006583101811

Titova, E. E., Di, V. I., Yurov, V. E., Raspopov, O. M., Trakhtengertz, V. Y., Jiricek, F., & Triska, P. (1984). Interaction between VLF waves and the turbulent ionosphere. *Geophysical Research Letters*, *11*(4), 323–326. Retrieved 2021-01-26, from http://agupubs.onlinelibrary.wiley.com/doi/abs/10.1029/GL011i004p00323 (_eprint: https://onlinelibrary.wiley.com/doi/pdf/10.1029/GL011i004p00323) doi: https://doi.org/10.1029/GL011i004p00323

Tröbs, M., & Heinzel, G. (2006, February). Improved spectrum estimation from digitized time series on a logarithmic frequency axis. *Measurement*, *39*(2), 120–129. Retrieved 2018-03-06, from http://www.sciencedirect.com/science/article/pii/S026322410500117X doi: 10.1016/j.measurement.2005.10.010

Wanliss, J. A., & Showalter, K. M. (2006). High-resolution global storm index: Dst versus SYM-H. *Journal of Geophysical Research: Space Physics*, *111*(A2). Retrieved 2021-01-25, from http://agupubs

.onlinelibrary.wiley.com/doi/abs/10.1029/2005JA011034 (_eprint: https://onlinelibrary.wiley.com/doi/pdf/10.1029/2005JA011034) doi: https://doi.org/10.1029/2005JA011034

Welch, P. (1967, June). The use of fast Fourier transform for the estimation of power spectra: A method based on time averaging over short, modified periodograms. *IEEE Transactions on Audio and Electroacoustics*, *15*(2), 70–73. doi: 10.1109/TAU.1967.1161901

Xia, Z., Chen, L., Zhima, Z., & Parrot, M. (2020). Spectral Broadening of NWC Transmitter Signals in the Ionosphere. *Geophysical Research Letters*, *47*(13), e2020GL088103. Retrieved 2021-01-25, from http://agupubs.onlinelibrary.wiley.com/doi/abs/10.1029/2020GL088103 (_eprint: https://onlinelibrary.wiley.com/doi/pdf/10.1029/2020GL088103) doi: https://doi.org/10.1029/2020GL088103

Yeh, K. C., & Liu, C.-H. (1982, April). Radio wave scintillations in the ionosphere. *IEEE Proceedings*, *70*, 324–360. Retrieved 2018-05-08, from http://adsabs.harvard.edu/abs/1982IEEEP..70..324Y

Zhao, S., Zhou, C., Shen, X., & Zhima, Z. (2019). Investigation of VLF Transmitter Signals in the Ionosphere by ZH-1 Observations and Full-Wave Simulation. *Journal of Geophysical Research: Space Physics*, *124*(6), 4697–4709. Retrieved 2021-01-25, from http://agupubs.onlinelibrary.wiley.com/doi/abs/10.1029/2019JA026593 (_eprint: https://onlinelibrary.wiley.com/doi/pdf/10.1029/2019JA026593) doi: https://doi.org/10.1029/2019JA026593